AMERICAN METEOROLOGICAL SOCIETY
AMS Journals Online

Full Text View

Seasonal Variability in the Equatorial Pacific

Xuri Yu

School of Oceanography, University of Washington, Seattle, Washington

Michael J. McPhaden

NOAA/Pacific Marine Environmental Laboratory, Seattle, Washington

ABSTRACT

Five to nine years of observations from the Tropical Atmosphere Ocean array in the tropical Pacific are used to document the seasonal cycle of surface winds, zonal currents, SST, thermocline depth, and dynamic height. Along the equator, the normally westward surface zonal current reverses direction in late boreal spring and early summer. This seasonal variation in the zonal surface current propagates westward, as do seasonal variations in the Equatorial Undercurrent and zonal surface winds at the equator. At 5°N and 5°S, the seasonal variations in the 20°C isotherm and dynamic height also propagate westward. Conversely at the equator in the eastern and central Pacific, the variations in 20°C isotherm depth and dynamic height propagate eastward.

These seasonal variations are interpreted by means of a simple dynamical model based on linear equatorial wave theory. Model results indicate that seasonal variability between 5°N and 5°S is dominated by wind-forced equatorial Kelvin waves and first meridional mode Rossby waves of the first and second baroclinic modes. The sum of the Rossby waves and Kelvin waves results in westward propagation in the equatorial zonal currents and off-equatorial thermal structure and, yet, eastward propagation in thermocline depth and dynamic height along the equator in the eastern and central Pacific.

1. Introduction

The seasonal cycle is a prominent mode of climate variability in the equatorial Pacific. It results ultimately from solar forcing, modified by coupled ocean–atmosphere–land interactions (Li and Philander 1996). Year-to-year variations in the

seasonal cycle are associated with El Niño and the Southern Oscillation (ENSO), a perturbation in the climate systems that affects the lives of millions of people around the globe. Warmest El Niño sea surface temperature (SST) anomalies in the equatorial cold tongue often occur in boreal winter (Rasmusson and Carpenter 1982). This seasonal phase locking of interannual SST anomalies suggests that the mean seasonal cycle exerts a significant control over the dynamics of ENSO (Xie 1995) and its predictability (Latif and Graham 1992; Webster and Yang 1992; Latif et al. 1994; Balmaseda et al. 1995). However few, if any, coupled ocean–atmosphere general circulation models are capable of simulating both the mean seasonal cycle and interannual ENSO-like variability with equal degrees of veracity (Mechoso et al. 1995). Therefore, a better description and understanding of the climatological mean seasonal cycle is necessary in order to accurately define interannual climate anomalies, to improve our knowledge about interactions between ENSO and mean seasonal variations, and to validate dynamical models under development for climate prediction.

Sea surface temperature is the primary oceanographic variable affecting the overlying atmosphere. A recurrent theme of empirical and modeling studies of the upper-ocean heat balance in the tropical Pacific is the importance of ocean dynamics in affecting SST variability (e.g., Seager et al. 1988; Hayes et al. 1991; Chang 1993, 1994; Chen et al. 1994; Kessler and McPhaden 1995). Previous studies have shown that the dynamics of seasonal timescale variability in the upper ocean are governed by the local response to wind forcing and by the excitation and propagation of Rossby and Kelvin waves (Meyers 1979a,b; Kindle 1979; Busalacchi and O'Brien 1980; Kessler 1990; Kessler and McCreary 1993; Minobe and Takeuchi 1995; Yang et al. 1997).

Certain aspects of the seasonal cycle, however, are still not well understood. Among these are the fact that winds, SST, and zonal currents along the equator propagate westward, while the 20°C isotherm depth along the equator propagates eastward in the central and eastern Pacific (e.g., Meyers 1979a, b; Horel 1982; Lukas and Firing 1985; McPhaden and Taft 1988; Kessler 1990). Based on XBT analysis, Meyers (1979a,b) first suggested that the eastward propagation in 20°C along the equator was due to equatorial Kelvin wave dynamics, whereas off-equatorial dynamics were governed by local Ekman pumping and westward propagating Rossby waves. Recent modeling studies support this basic hypothesis (Minobe and Takeuchi 1995; Yang et al. 1997), although there are ambiguities among these recent studies on how precisely annual-period equatorial Kelvin and Rossby waves combine to produce the full range of observed variability near the equator.

Another aspect of the mean seasonal cycle that is not fully understood is the springtime reversal of the South Equatorial Current (SEC) in the eastern equatorial Pacific. This reversal of the normally westward flowing SEC was first observed by Puls (1895) in ship drift data and later confirmed from moored time series data (Halpern 1987; McPhaden and Taft 1988). Several hypotheses have been proposed for why the SEC runs counter to the easterly trade winds in the eastern Pacific; these hypotheses typically involve various combinations of local wind forcing, equatorial Kelvin wave dynamics, and/or seasonal modulation of high-frequency instability waves (Philander et al. 1987; McPhaden and Taft 1988; Philander and Chao 1991; Yu et al. 1997). The relationship of the springtime reversal to other aspects of the seasonal cycle, for example, the prominent annual Rossby wave, has not been fully clarified however.

The purpose of this study is to examine the dynamics of the mean seasonal cycle in the tropical Pacific, addressing the specific issues raised above. We will rely primarily on data from the Tropical Atmosphere Ocean (TAO) Array, which has grown from a few moorings in the early 1980s to a network of about 70 moorings spanning the equatorial Pacific basin between about 8°N and 8°S (McPhaden 1995). Many of the sites have been instrumented for a sufficiently long period (more than five years) to compute reliable monthly mean climatologies.

There are several advantages of using TAO data for this study. One is that high-frequency variability that might otherwise be aliased in infrequent shipboard measurements can be averaged out, yielding more sharply defined features of the mean seasonal cycle. Another is that contemporaneous data for winds, SST, and upper-ocean temperatures are available, all with similar temporal/spatial resolution and covering large regions not routinely sampled by standard shipping routes. Finally, unique to the TAO data is the ability to compute climatologies of upper-ocean velocity at several mooring sites along the equator (qv McPhaden and McCarty 1992; McCarty and McPhaden 1993).

The remainder of this paper is outlined as follows. Section 2 describes the datasets and processing procedures used in this study. Section 3 presents means and mean seasonal variations computed from TAO data and compares TAO mean seasonal variations with climatologies based on ship winds, upper-ocean thermal data, drifting buoys, and blended in situ–satellite SST analyses. These comparisons are performed as a check on the representativeness of the TAO climatologies, which are based on relatively short records. Diagnosis of the mean seasonal cycle in terms of wind-forced Kelvin and Rossby waves will be presented in section 4, followed by a discussion and summary of the important conclusions of this study in section 5.

2. Data and processing

We rely most heavily in this study on data from the TAO buoy array (McPhaden 1993). We also will use several other datasets to compare with the seasonal cycle computed from TAO data to determine the representativeness of TAO seasonal analyses relative to those based on longer term records. These other datasets are the Florida State University (FSU) winds

(Legler 1991), Reynolds and Smith SST (Reynolds and Smith 1995), Reverdin surface currents (Reverdin et al. 1994), and Levitus temperatures (Levitus et al. 1994b). TAO observations are included in some of these other datasets, but they represent a relatively small percentage of the overall data in these datasets. Therefore, our comparisons will not be overly biased by this overlap. There are other surface wind, temperature, and current products to which we could compare the TAO analyses, but the above climatologies are representative and sufficient for our purposes. In this section, we will describe the TAO dataset in detail and then briefly introduce the other datasets.

a. The TAO buoy array

The TAO array was implemented as part of the TOGA program for improved description, understanding, and prediction of seasonal-to-interannual climate variability. The array presently consists of nearly 70 deep ocean moorings with 2°–3° meridional spacing and 10°–15° longitudinal spacing across the equatorial Pacific, spanning from 8°S to 8°N (McPhaden 1995) (Fig. 1 ⊙🔲). Most of these buoys are Autonomous Temperature Line Acquisition System (ATLAS) thermistor chain moorings (Hayes et al. 1991), which measure temperatures at the surface and 10 subsurface depths down to 500 m, as well as surface winds, relative humidity, and air temperatures.

In addition, the TAO array includes a small number of current meter moorings along the equator, collecting time series of currents down to depths of 250–300 m (McPhaden 1993). The current meter measurements are obtained from both mechanical current meters (MCMs) and acoustic Doppler current profilers (ADCPs), depending on site. At 110° and 140° W, we rely primarily on MCM data because of problems with fish bias in the acoustic signals (Plimpton et al. 1997a). At 170°W, only ADCP data are available (Weisberg and Hayes 1995; Plimpton et al. 1997b). At 165°E, we rely primarily on mechanical current meter data since these records are the longest; however, we fill gaps with ADCP data (which are not significantly affected by fish bias at this site) when available.

We make use primarily of daily averaged TAO data in this study. These averages are based on measurements at sampling intervals ranging from 10 min to 1 h. Details of sampling characteristics, instrumentation, and measurement errors can be found in McPhaden and McCarty (1992), McCarty and McPhaden (1993), Mangum et al. (1994) and Plimpton et al. (1997a,b).

We compute mean climatologies of surface pseudostress, temperature, and current by using the records from the locations where the buoys had operated for more than five years by the end of 1996, restricting ourselves to the period 1988–96, which encompassed most of the growth in the TAO array. Longitudinally, we limit ourselves to the region 165°E–110°W. Although there are sites along 156°E that were occupied during 1991–96, the records at this longitude are gappy and the seasonal cycle is too weak to be reliably extracted with confidence from records only five years long.

For those sites retained in our analysis, we compute the mean seasonal cycle in the following manner. First, we average the daily averaged time series to monthly means. Second, we average monthly means of each individual month of the year over the time period of January 1988–December 1996. Lastly, the resulting monthly climatologies are smoothed by a 1–2–1 filter to remove the intraseasonal variability (Kessler and McPhaden 1995; Kessler et al. 1995). For the mean climatology of surface pseudostress (defined as $|\mathbf{U}|\mathbf{U}$, where $\mathbf{U}$ is the vector wind speed), we first compute the pseudostress from the daily averaged surface winds before computing the seasonal cycle.

In addition, we compute a mean climatology of dynamic height relative to 500 dbar. Daily averaged temperatures are used to compute dynamic height with salinity information provided by a mean temperature–salinity relationship based on the Levitus et al. (1994a) and Levitus et al. (1994b) temperature and salinity climatologies. The error for the calculation is about 3–4 dyn cm in the western Pacific and 2–3 dyn cm in the eastern Pacific, mainly due to the use of the mean temperature–salinity relationship, neglected variability below 500 dbar, and relatively coarse vertical resolution of the TAO temperature observations (Busalacchi et al. 1994).

Ninety percent confidence intervals for each individual month of the climatology are estimated based on the Student's t-distribution, assuming that each year is independent. The standard deviation for each month required in this calculation is estimated from year-to-year variations around the sample mean for a given month, so the estimated errors are mainly due to interannual variability around the mean climatology.

To analyze the characteristics of seasonal variations, the monthly mean climatologies are fit to a five-parameter harmonic regression model for annual means, and 1 and 2 cycle per year (cpy) harmonics. Error variances are computed from residuals around these regressions, assuming 7 degrees of freedom (12 months less than 5 parameter fit). Standard errors for means, amplitudes, and phases of the harmonics are derived using standard formulas (Draper and Smith 1981).

In addition to random sampling errors, a potential source of bias error enters into our calculation of near-surface currents at 0°, 170°W. Measurements at this location were made primarily with upward-looking ADCPs mounted on subsurface floats at depths between 250 and 300 m. Side-lobe reflections from the surface contaminate the upper 10% (25–30 m) of

the profile, so velocities at depth 10–20 m were computed by linear extrapolation of the vertical gradient from deeper levels, as in Weisberg and Hayes (1995). We tested the accuracy of this procedure using data at 0°, 140°W where an extrapolated time series could be compared with an actual 10-m time series. Actual and extrapolated time series of monthly mean zonal velocity had a cross-correlation coefficient of 0.96, and the standard deviation of the differences was about 6 cm s^{-1}. However, the record length mean of the extrapolated time series was too strong to the west by 11 cm s^{-1}. Whereas vertical shears on which this extrapolation is based are stronger at 140°W than 170°W, the test nonetheless points out a potential for our shallow 10–20-m velocity estimates at 0°, 170°W to be biased westward by several centimeter per second.

b. The Florida State University wind product

The FSU wind product is a monthly analysis of ship and buoy winds on a 2° × 2° grid over the tropical Pacific (Legler 1991). Its mean climatology is computed in the same manner as from TAO winds, but for two different lengths of records. One is averaged over 36 years from January 1961 to December 1996. Another is averaged over 1988–96, that is, the same period as the TAO climatology. In addition to making comparisons between TAO and FSU pseudostress, we will use the FSU product to force a Kelvin wave characteristic model (section 4).

We note that FSU analysis procedures do not take into account the different anemometer heights of the various sources of wind information from ships and buoys (D. Legler 1997, personal communication). Thus, we will make no adjustments to either climatology when making our comparisons. If the FSU climatology were representative of winds at 10-m height, the computed pseudostresses based on TAO buoy winds at 4-m height might be 15% weaker than the FSU winds under conditions of neutral stability. This difference is no larger than uncertainties in drag coefficients used to compute stresses and would not fundamentally alter our conclusions about the degree of consistency between the two climatologies.

c. Levitus et al. temperature climatology

This dataset is an objective analysis of all historical temperature data between 1900 and 1993. Data sources include the National Oceanographic Data Center (NODC) archives, the NODC Oceanographic Data Archaeology and Rescue project, and the Intergovernmental Oceanographic Commission Global Oceanographic Data Archaeology and Rescue project (Levitus et al. 1994b). The data consist primarily of vertical profiles from expendible bathythermographs, conductivity–temperature–depth, mechanical bathythermograph casts, and digital bathythermograph casts. The irregularly sampled data are mapped to standard depth levels through Lagrangian interpolation and then binned into 1° lat by 1° long squares with optimum interpolation described in Gandin (1966). To produce climatological means, all the historical data in a given one-degree square within a given month are averaged as a representative of the monthly mean for the square. Various techniques are used to quality control the data. Errors in analyzed fields are usually less than 1°C in the Pacific Ocean.

d. Reynolds and Smith SST

This dataset is a monthly 1° global sea surface temperature climatology constructed from two intermediate climatologies (Reynolds and Smith 1995). The first is for a 30-yr (1950–79) period between roughly 40°S and 60°N based on in situ (ship and buoy) SST data, supplemented by 4 years (1982–85) of satellite SST retrievals. The second is based on monthly analyses using in situ SST data, satellite SST retrievals, and sea ice coverage data over a 12-yr period (1982–93). Uncertainties in SSTs from this climatology are typically about 0.6°C.

e. Reverdin surface currents

This gridded dataset is constructed as described by Reverdin et al. (1994) from current data during the period January 1987 to April 1992. The records from more than 1000 surface drifting buoys are merged with currents from TAO current-meter moorings at five sites (four along the equator at 165°E, 170°W, 140°W, and 110°W and one at 7°N, 140°W). These data are optimally fitted into regular grids of 1° lat by 5° long. The drifters were initially drogued at 15 m. Sampling errors due to high-frequency variations are of the order of 7 cm s^{-1} at most except near the boundaries; systematic error can exceed 5 cm s^{-1} near 20°N and 20°S.

3. TAO climatologies and intercomparisons

In this section, we first describe mean surface winds, temperatures, currents, and surface dynamic height from the TAO array, then the seasonal variations around these means. Comparisons with other datasets will then be made for seasonal variations in order to examine the consistency of the TAO climatologies relative to those from other observational datasets.

a. Means of TAO observations

Figure 2 ⊙= shows the longitudinal profiles of mean zonal and meridional winds and surface dynamic height (0/500 db), and the longitude–depth contours of temperature and zonal current means along the equator. Sea surface temperature decreases to the east, from 29°C at 165°E to 23°C at 110°W. The coldest SSTs are found in the eastern Pacific where the thermocline is shallow and equatorial upwelling is efficient at cooling the surface. The thermocline slopes upward toward the east in response to zonal wind stress forcing (Fig. 2a ⊙=). Using the 20°C isotherm as an indicator, thermocline depth decreases from about 160 m at 165°E to about 50 m at 110°W (Fig. 2c ⊙=). Surface dynamic height rises to the west by about 40 dyn cm, likewise in response to zonal surface wind stress forcing.

The core of the eastward Equatorial Undercurrent (EUC) slopes upward to the east in the thermocline (Fig. 2d ⊙=) with maximum flow around 140°W. The undercurrent is driven by the eastward zonal pressure gradient, which in turn is set up by the surface easterlies (McPhaden 1981; McCreary 1981). The surface South Equatorial Current along the equator is toward the west, in the direction of the surface wind stress. Maximum westward flow in the SEC occurs at 0°, 170°W. This maximum is probably real but may be accentuated by a westward bias in mean currents of several centimeters per second as described in the previous section. The magnitude of the SEC is much weaker than that of the undercurrent, even though the SEC is directly forced by the stress. Philander and Pacanowski (1980) argued that the westward momentum generated by the surface stress is reduced by vertical advection of eastward momentum due to upwelling, resulting in the weaker surface current than one would expect from linear theory (McPhaden 1981; McCreary 1981). Diagnostic analyses of the mean zonal momentum balance are consistent with this hypothesis (Bryden and Brady 1985; McPhaden and Taft 1988).

The meridional–depth structures of temperature at 165°E, 140°W, and 110°W are shown in Fig. 3 ⊙=. The most prominent feature at 140° and 110°W is shoaling of isotherms toward the equator in the upper 50–100 m, which indicates that cold water is brought up to the surface layer by trade-wind-forced equatorial upwelling. At 165°E, the effects of upwelling are not evident because the easterly surface stress is very weak and the thermocline is relatively deep. Another important feature, shown in all three locations, is vertical stretching of the thermocline near the equator. This feature is associated with the geostrophic shear of the westward surface current and eastward undercurrent current in the thermocline (Lukas and Firing 1983).

b. Seasonal variations of TAO observations

Figure 4 ⊙= displays time series of the monthly mean climatologies of surface winds and surface dynamic height (0/500 db), and the depth–time structure of the climatologies of temperatures and zonal currents at 165°E, 170°W, 140°W, and 110°W at the equator. The seasonal variation in both zonal and meridional winds is much larger in the eastern Pacific than in the western Pacific (Fig. 4 ⊙=, upper panels). In the eastern Pacific, the winds are from the southeast quadrant with minimum speeds in boreal spring and maximum speeds in boreal fall or winter. The variation of meridional winds is out of phase with the zonal component in the eastern Pacific, that is, weak easterlies are associated with weak southerlies and vice versa. SST in the eastern Pacific ocean undergoes a prominent seasonal variation; its range is 2°–3°C, with highest temperatures in boreal spring and lowest in boreal fall (Figs. 4c and 4d ⊙=). In the western Pacific, where the surface winds have very weak seasonal variability and the thermocline is deep, the seasonal variation in SST is much weaker.

The upper thermocline undergoes its largest seasonal vertical migration in the central and eastern Pacific; west of the date line these migrations are of much smaller amplitude (Fig. 4 ⊙=). At 170°W, the thermocline begins to shoal in January and is at its shallowest in May–June (Fig. 4b ⊙=, lower middle panel). At 140° and 110°W, the thermocline starts to shoal in late January, but it does not reach its shallowest depth until June–July at 140°W and August at 110°W. The seasonal range in surface dynamic height is typically less than 15 dyn cm, with minima (maxima) surface heights corresponding roughly to periods of shallowest (deepest) thermocline depth.

The zonal surface current has significant seasonal variations at all four locations (Fig. 4 ⊙=, lower panels) with a largest magnitude in the eastern Pacific. In boreal spring, the current flows eastward at speeds of 20–30 cm s^{-1} at 140° and 110°W while the surface zonal winds, although weaker, are still easterly. This "springtime reversal" of the SEC reaches its maximum in April at 110°W and in May at 140°W. Farther west at 170°W, 10-m currents nearly reverse in June (and may actually reverse when taking account of the probable westward bias in our estimated 10-m mean flow at this site), while at 165°E zonal velocity reverses and flows against the surface winds in June–August. At both 170°W and 165°E there is also a prominent semiannual component to the 10-m zonal velocity, which at 165°E results in a second period of eastward flow in November–January.

Zonal currents from the surface to the EUC core vary seasonally in phase (Fig. 4 ⊙=). In boreal spring, the EUC reaches its maximum in the eastern Pacific of about 120 cm s^{-1} at 140°W and about 105 cm s^{-1} at 110°W. Also the EUC core undergoes a seasonal vertical migration, reaching its shallowest depths in boreal spring (~ 80 m at 140°W and ~ 60 m at 110°W) and its deepest depths in early boreal winter. At 170°W, the scenario is similar but the variations lag those farther to the east. The seasonal variation of the EUC is relatively weak at 165°E compared to farther to the east, though still apparent with a maximum in boreal spring at a depth of around 200 m.

Seasonal variations in winds, temperature, dynamic height, and zonal current are highlighted by subtracting the long-term means from monthly mean climatologies (Figs. 5 ⊙ and 6 ⊙). Along the equator, zonal winds progress westward, as do SST and zonal currents in both the surface and subsurface layers. In contrast, vertical displacements of the 20°C isotherm and dynamic height have a different character east and west of about 170°W. East of this longitude, a dominant annual period fluctuation propagates eastward, whereas west of 170°W there is a suggestion of westward propagation and a more pronounced semiannual cycle.

The time–longitude structure of the seasonal variability in 20°C isotherm depth and surface dynamic height along 5°N shows very clear westward propagation across the entire basin (Figs. 6c and 6d ⊙). At 5°S, westward propagation is also apparent in 20°C and dynamic height primarily west of 140°W. Using the NCEP/ODAS (Ocean Data Assimilation System) reanalysis data, Wang et al. (1999, manuscript submitted to *J. Climate*) show similar phase propagation in thermocline depth variations along 5°N and 6°S.

Meridional wind stress tends to propagate eastward in the western and central Pacific (Fig. 5b ⊙). However, meridional wind stress is relatively inefficient at exciting dynamical responses in the equatorial ocean on seasonal timescales (Gent et al. 1983), so hereafter we will focus discussion primarily on zonal wind stress.

To further analyze the seasonal cycle, monthly mean climatologies are fit to a five-parameter (annual mean, 1 cpy and 2 cpy) harmonic regression model. Then the phases and amplitudes of the harmonics are used to estimate their zonal phase speeds using an amplitude-weighted linear least squares fit. We note that the 1 cpy harmonic is generally larger than the 2 cpy harmonic, and the amplitude of the 2 cpy harmonic exceeds one standard error less often than the amplitude of the 1 cpy harmonic (not shown). Therefore, in subsequent discussion, we will emphasize 1 cpy variations, noting where appropriate the importance of 2 cpy variations in the seasonal cycle.

The annual harmonic typically has its maximum amplitude in the eastern and central Pacific, and phase increases to the west in all the variables except the 20°C isotherm and dynamic height along the equator (Figs. 7b ⊙ and 8b ⊙). The annual harmonic of zonal pseudostress has its maximum amplitude in the eastern Pacific (Fig. 7a ⊙), with a zonal phase speed of -0.43 ± 0.13 m s^{-1} (Table 1 ⊙). The annual harmonic of SST has significant amplitude only east of the date line; its phase increases to the west with a phase speed of -0.87 ± 0.23 m s^{-1}. Annual harmonics of surface zonal current and 80-m zonal current have significant amplitude across the entire region 165°E–110°W (Fig. 7a ⊙) with phase speeds -0.73 ± 0.27 m s^{-1} and -1.13 ± 0.45 m s^{-1}, respectively.

Annual period fluctuations in 20°C depth and dynamic height along the equator are largest in the central Pacific. Conversely, amplitudes at 165°E are only marginally significant and the phases there are highly uncertain. For that reason, phase speeds for the annual harmonic in 20°C depth and dynamic height cannot be reliably estimated in the western Pacific. For the eastern and central Pacific where 20°C isotherm depths and dynamic height amplitudes are highly significant, phase speeds along the equator are eastward at 0.5–0.7 m s^{-1} (Table 1 ⊙).

The annual harmonic of 20°C isotherm depth and dynamics height is larger at 5°N than at either 0° or 5°S. This is probably due to the stronger seasonal wind stress and wind stress curl forcing north of the equator (e.g., Gent 1985; McPhaden et al. 1988; also see more discussion in section 4). Phase speeds are westward at about 1 m s^{-1} on average at both 5°N and 5°S (Table 1 ⊙). The relatively large uncertainty in phase speeds at 5°S results from the lack of zonal phase progression east of 140°W. Nevertheless, at both 5°N and 5°S, these phase speeds are significantly different from the eastward phase speed in 20°C and dynamic height along the equator of roughly 0.5–0.7 m s^{-1}.

c. Comparison with other climatologies

The zonal surface pseudostress along the equator from the TAO array is consistent with FSU pseudostress (Figs. 9a and 9b ⊙). In both, variations progress to the west with a similar phase speed (Table 1 ⊙), but with relatively larger amplitudes in the TAO data. The amplitude difference could be due to the fact that FSU mean climatology is averaged over 1961–96 while the TAO mean climatology is averaged over only 1988–96. Indeed, the amplitude of the seasonal variability is more consistent with that in the TAO climatology in the eastern Pacific if the FSU climatology is averaged over the same period as the TAO data. Lukas and Firing (1985) also analyzed the surface winds collected during the Hawaii-to-Tahiti Shuttle experiment from ship, buoys, satellite, and island weather stations. The annual harmonic amplitude is about 30% weaker in their analysis than in our analysis of TAO observations, but the phase speed of -0.41 m s^{-1} they obtained is essentially identical to our estimate of -0.43 m s^{-1}, considering the uncertainties in the calculations.

Variations in SST from the TAO array are similar to those of Reynolds SST along the equator, capturing the major large zonal-scale features such as westward phase progression and magnitude of seasonal cycle (Figs. 9c and 9d ⊙). The two

analyses agree particularly well in the central and eastern Pacific, where seasonal variability is largest. The Reynolds SST shows a slower westward phase progression than TAO west of 160°W, but in this region seasonal variations in both products are weak.

Figure 9 🔘▬ also displays longitude–time contours of zonal surface current along the equator from the TAO buoy array and the Reverdin et al. near-surface velocity analysis. Both analyses show similar large-scale features, including westward propagation of the annual cycle and a 2 cpy variation in the western Pacific. The zonal phase speed of the annual cycle in the Reverdin et al. zonal currents along the equator is -0.59 m s^{-1}, comparable to the phase speed from our analysis of TAO buoy data (Table 1 🔘▬). There are no subsurface current climatologies against which to compare those from the TAO array.

Figure 10 🔘▬ compares the TAO climatology for the 20°C isotherm depth with the Levitus temperature analysis, both on and off the equator. The best agreement is along 5°N, both in amplitude and phase. At 5°S, TAO and Levitus amplitudes are similar, but the Levitus analysis shows a more consistent westward phase increase across the basin, particularly east of 140°W. Least squares determined phase speeds for the TAO and Levitus analyses are nearly identical at 5°S, but the greater consistency of the Levitus phase progression leads to more reliable phase speed estimates at this latitude (Table 1 🔘▬). It may be that TAO record lengths of typically 5–6 years are insufficient to extract subtleties of phase characteristics in the southeastern equatorial Pacific where annual-period signals are relatively weak.

Along the equator, both TAO and Levitus datasets exhibit eastward phase propagation at about 0.5–0.7 m s^{-1} for the annual harmonic in the central and eastern Pacific (Figs. 10a,b 🔘▬; Table 1 🔘▬). Likewise both suggest westward propagation and a relatively strong semiannual cycle in the western Pacific. In the Levitus data, the dividing longitude between eastward and westward phase propagation along the equator (around 155°W) is more strongly demarcated than in the TAO data, probably due to the better zonal resolution in the Levitus analysis. Other detailed differences are evident, but these are not unexpected given the differences in data sources and data distributions for the TAO and Levitus climatologies.

In summary, TAO data are used to document well-defined mean seasonal cycles, consistent with other climatologies, all of which are compiled from much longer records except the Reverdin surface currents. In some cases quantitative differences arise, but these differences are of secondary importance compared to the basic similarities in the respective climatologies.

4. Diagnosis of dynamics

As shown in the previous section, seasonal variability in the 20°C isotherm depth and surface dynamic height at both 5°N and 5°S propagates westward with a phase speed of about 1 m s^{-1}. Equatorial zonal currents also propagate to the west with a similar phase speed. In contrast, variability in 20°C isotherm depth and dynamic height along the equator propagates eastward with phase speeds of about 0.5–0.7 m s^{-1} in the eastern and central Pacific.

In some previous studies (Meyers 1979b; Kessler 1990), westward propagation in thermal structure on seasonal timescales at ±5° was interpreted as first baroclinic mode midlatitude (i.e. quasigeostrophic) Rossby waves. The quasigeostrophic approximation has the advantage of simplifying diagnostic equations for upper-ocean thermal structure in that the vorticity balance can be localized and evaluated at a single latitude. However, at low latitudes, scale analysis indicates that quasigeostrophy is not strictly valid as the Coriolis force becomes vanishingly small near the equator. Linear theory predicts that fluctuations on timescales longer than about one day become trapped in an equatorial waveguide, and that within this waveguide variability is coherent across a range of latitudes. Consistent with this theory, recent studies of seasonal variability in the equatorial Pacific (e.g., Kessler and McCreary 1993; Minobe and Takeuchi 1995) have been successful in the application of equatorial wave principles to the interpretation of model results and ocean observations.

Our observations of coherent westward propagating velocity and temperature structures between 5°N and 5°S likewise argue for an interpretation in terms of equatorial wave dynamics. Specifically, we hypothesize that much of the observed westward propagation in ocean variables between 5°N and 5°S is due to long, nondispersive equatorial Rossby waves. Other equatorial wave modes must be responsible, however, for eastward propagation of thermocline depth observed along the equator. The only logical candidate at low frequency is the equatorial Kelvin wave. We can exclude short Rossby waves and mixed Rossby gravity waves from consideration because their phase speeds are westward and their zonal wavelengths are on the order of hundreds, rather than thousands, of kilometers.

Observed eastward phase speeds in 20°C depth and dynamic height along the equator do not correspond to low baroclinic-mode free Kelvin wave speeds based on linear theory, as will be elaborated on below. We will find that these phase speeds result in part from a mix of Kelvin and long, nondispersive Rossby wave modes. In addition, wind forcing is prevalent along the entire zonal extent of the basin. Under these circumstances, variability at a particular location will result from both local and remote forcing.

In this section, we present a simple model to simulate wind-forced Kelvin and Rossby wave variability based on the equatorial wave characteristics. The model was first developed by Gill and Clarke (1974), using only winds and mean ocean density structure as input. Following McCreary (1981), we will modify this model to incorporate damping. Recently, Minobe and Takeuchi (1995) used this model to simulate seasonal wave variability in the equatorial Pacific. Like them, we will conclude that the two gravest baroclinic-mode Kelvin waves and the first meridional mode Rossby waves of the first two baroclinic modes dominate at the seasonal cycle within 5° of the equator. In addition, using this formalism we quantitatively demonstrate why zonal currents propagate westward, but thermal structure tends to propagate eastward along the equator in the eastern and central Pacific.

a. Estimates of Kelvin and Rossby wave variability

Following McCreary (1981), the momentum and continuity equations for a vertical baroclinic mode are

$$\left(\frac{\partial u_n}{\partial t} + \frac{A}{c_n^2} u_n\right) - \beta y v_n + \frac{\partial p_n}{\partial x} = \frac{\tau^x}{\rho \int_{-H}^{0} \psi_n^2 \, dz} \quad (1a)$$

$$\beta y u_n + \frac{\partial p_n}{\partial y} = \frac{\tau^y}{\rho \int_{-H}^{0} \psi_n^2 \, dz} \quad (1b)$$

$$\left(\frac{\partial}{\partial t} + \frac{A}{c_n^2}\right)\frac{p_n}{c_n^2} + \frac{\partial u_n}{\partial x} + \frac{\partial v_n}{\partial y} = 0, \quad (1c)$$

where u and v are zonal and meridional velocities, p is kinematic pressure, c_n is the eigenvalue for the nth vertical mode, A is a constant related to the vertical friction and diffusion, H is the full depth of the ocean, (τ^x, τ^y) is the surface wind stress, and ψ_n is the nth vertical structure function, determined by solution of a Sturm–Liouville eigenvalue problem. We have made the long-wave approximation by neglecting $(\partial_t + A/c_n^2)v_n$ in (1b). This approximation filters out all equatorial waves except low-frequency Kelvin waves, which propagate nondispersively eastward, and long Rossby waves, which propagate nondispersively westward.

Wind-forced equatorial waves can be written as

$$u_{mn} = S_{mn}(x, z, t)\phi_0(y) \quad (2a)$$

$$p_{mn} = c_n S_{mn}(x, z, t)\phi_0(y) \quad (2b)$$

for Kelvin waves (with $m = -1$) and

$$u_{mn} = S_{mn}(x, z, t)\left(\sqrt{\frac{m}{m+1}}\phi_{m+1}(y) - \phi_{m-1}(y)\right) \quad (3a)$$

$$p_{mn} = c_n S_{mn}(x, z, t)\left(\sqrt{\frac{m}{m+1}}\phi_{m+1}(y) + \phi_{m-1}(y)\right) \quad (3b)$$

for Rossby waves (with $m \geq 1$). The index m is a meridional mode number and ϕ_m is a Hermite function of order m. The ϕ_m implicitly depend on vertical mode number n through scaling of the latitudinal coordinate y by the equatorial Rossby radius of deformation

$$\lambda_n = (c_n/\beta)^{1/2}. \quad (4)$$

The meridional structures of u and p for the Kelvin wave and first two meridional mode Rossby waves, determined by Φ_m, are shown in Fig. 11 〇–.

The $S_{mn}(x, z, t)$ for a wave mode (m, n) is an integral over wind projection onto this mode, expressed as

$$S_{mn}(x, z, t) = S_{mn}\left[X, t + \frac{(X - x)}{c_n}\right]$$

$$+ \alpha_n(z) \int_X^x b_{mn}\left[\xi, t + \frac{(\xi - x)}{c_n}\right]$$

$$\times \exp[-r_n(x - \xi)] \, d\xi, \quad (5)$$

where X is the western (eastern) boundary for Kelvin (Rossby) waves, r_n is a damping coefficient, $\alpha_n(z)$ is an amplitude of coefficient, and b_{mn} is the projection of the winds onto the wave mode. At low-frequency limit, the b_{mn} can be expressed as (Gill and Clarke 1974)

$$b_{-1n} = \frac{1}{\sqrt{2}} \int_{-\infty}^{+\infty} \frac{\phi_0(y) \tau^x(x, y, t)}{\lambda_n} \, dy \quad (6a)$$

for Kelvin waves and

$$b_{mn} = \int_{-\infty}^{+\infty} \left[\frac{\phi_{m+1}(y)}{\sqrt{m+1}} - \frac{\phi_{m-1}(y)}{\sqrt{m}}\right] \frac{\tau^x(x, y, t)}{\lambda_n} \, dy \quad (6b)$$

for Rossby waves. The total ocean response to the wind forcing is the sum of all these waves, that is, $\Sigma^{\infty}_{n=1} (\Sigma^{\infty}_{m=1} S_{mn} + S_{-1n})$.

Here $S_{mn}(x, z, t)$ can be any dependent variable as specified by the coefficient $\alpha_n(z)$. For the pressure and zonal velocity, $\alpha_n(z)$ is (Kessler and McPhaden 1995), respectively,

$$\alpha_n^p(z) = \frac{\psi_n(0)\psi_n(z)}{\rho H}$$

$$\alpha_n^u(z) = \frac{\psi_n(0)\psi_n(z)}{\rho c_n H},$$

where ρ is water density. The first term in (5) is the wave amplitude at the western (eastern) boundary for a Kelvin (Rossby) wave.

In this study, the $\psi_n(z)$ and c_n are estimated from the Hawaii–Tahiti Shuttle experiment, which took place between 150° and 158°W (Kessler and McPhaden 1995). The $\psi_n(z)$ were obtained assuming a surface mixed layer of 75-m depth. The values of the first four modes are shown in Fig. 12 〇– and Table 2 〇–, with H assumed to be 4000 m. The seasonal cycle of winds from TAO observations is available only from 165°E to 110°W, so we use linearly interpolated daily values of FSU winds to force the model. With the time step (Δt) of one day, the zonal resolution (Δx) is set at 2° to satisfy the numerical stability criterion $\Delta t < \Delta x/c_n$.

The integral in (6) is taken only over 13°S–13°N to avoid problems with land masses at higher latitudes. However, these limits of integration are sufficient because the e-folding latitude of $\Phi_m(y)$ is significantly less than 13° for a few gravest meridional modes.

For forced Kelvin waves, the eastward integral along the wave characteristic in (5) starts at 150°E where the land effect is not significant. For forced Rossby waves, the westward integral starts at 80°W. These integrations along wave characteristic paths will involve negative time (i.e., $t + (\xi - x)/c_n < 0$). When this occurs, 12 months will be added to the time since a seasonal cycle is periodic. This approach is similar to initializing an ocean numerical model with mean climatology winds for several years.

The drag coefficient and air density we use to convert FSU pseudostress to stress are 1.2×10^{-3} and 1.2 kg m^{-3}. The damping coefficient is a variable function of vertical mode n with specific values given by

$$r_n = A/c^2_n = (c_1/c_n)^2 \ (6 \ \text{months})^{-1}. \tag{7}$$

This equation yields values of $r_1 = (6 \ \text{months})^{-1}$ and $r_2 = (2.5 \ \text{months})^{-1}$, similar to those recommended by Picaut et al. (1993).

We begin by considering only the gravest baroclinic and meridional modes to clearly illustrate the importance of wave dynamics in the seasonal cycle. Specifically, we initially limit our calculations to the Kelvin wave and first meridional mode Rossby wave of the first four baroclinic modes. How higher baroclinic and meridional modes affect the solutions are considered in sections 4e and 4f. We also initially limit ourselves to considering just forced wave solutions in the interior ocean, since previous studies (e.g., Kessler and McCreary 1993; Minobe and Takeuchi 1995) have suggested that boundary reflections are of secondary importance for the mean seasonal cycle in the equatorial Pacific. Boundary reflections will be considered explicitly in section 4c, where we show that they are weak in the longitude range sampled by the TAO array.

b. Wind-forced waves

Figure 13 ⬤ shows the sum of the first four baroclinic-mode Kelvin waves for zonal surface current and sea level along the equator from the model (top panels). Sea level has been computed by dividing surface pressure by $\rho_o g$. Both the current and sea level have consistent eastward propagation. The first and second vertical modes explain 38% and 53% of the simulated zonal velocity variance at the surface, respectively, while the third and fourth modes together explain only 9% of the simulated variance. For sea level, the first two baroclinic modes explain 60% and 38% of the simulated variance, respectively.

The sum of the four gravest vertical modes for first meridional mode Rossby waves shows consistent westward propagation along the equator (Fig. 13 ⬤, middle panels). The first mode explains 76% of total variance in simulated sea level; the second explains 19% of the total variance. Similarly, the first two vertical mode Rossby waves explain 63% and 29% of the variance in the simulated surface zonal velocity, respectively. Therefore, for both Kelvin and Rossby waves, the two gravest vertical modes are dominant in seasonal variability along the equator. However, for zonal velocity, Rossby waves together have larger amplitude than Kelvin waves, particularly in the central Pacific. For sea level, on the other hand, amplitude of the Kelvin waves is usually larger.

The combination of Kelvin and Rossby waves from the model is also shown in Fig. 13 ⬤ (bottom panels). Despite the simplicity of the model, zonal velocity and sea level are in general comparable to those in the observations (cf. Figs. 5c ⬤ and 6b ⬤). Along the equator, the model exhibits westward propagation of zonal currents with a seasonal cycle similar to that observed. Sea level propagates eastward east of about 160°W and westward west of that longitude. For comparison with the phase speeds in Table 1 ⬤, model surface zonal currents propagate westward at -0.66 ± 0.13 m s^{-1} and model sea level propagates eastward at 0.52 ± 0.12 m s^{-1} between 155° and 110°W. There are differences between the model and the observations as one might expect, but these are not so large as to obscure the essential similarities. In particular, the modeled currents are too strong with extrema centered near 140°W rather than 110°W as in the observations. Also, the 1 cpy amplitude in sea level due to the Rossby waves is too large in the western Pacific.

Observations at ±5° can also be compared with the wave model. At ±5° Kelvin wave variability is only 28% (14%) of the maximum at the equator for the first (second) vertical mode (Fig. 11 ⬤) so that variability at these latitudes should be dominated by Rossby waves. The average of dynamic height at 5°N and 5°S, namely,

$$\text{dyn}(5°) = 0.5[\text{dyn}(5°\text{N}) + \text{dyn}(5°\text{S})], \tag{8}$$

is mainly due to meridionally symmetric long Rossby waves and should have similar phase features to Rossby wave variability at the equator. This is indeed the case, comparing the simulated Rossby waves in Fig. 13 ⊙ with dyn(5°) derived from both the TAO data and Levitus analysis (Fig. 14 ⊙).

From these results, we can explain the strikingly different phase in zonal currents, dynamic height, and thermocline depth along the equator for the seasonal cycle. Rossby and Kelvin wave contributions to the pressure field are roughly comparable in magnitude, with eastward propagating Kelvin wages having greater influence in the east and westward propagating Rossby waves having greater influence in the west. However, for zonal velocity west of 120°W, Rossby wave amplitudes exceed Kelvin wave amplitudes so that westward propagation in zonal velocity is evident over a much broader range of longitudes.

Why do Rossby waves explain more variance in zonal currents than Kelvin waves? It is related to the differences in the relationship between zonal velocity and pressure for these two waves (Fig. 11 ⊙). Specifically, for a Kelvin wave, the ratio of pressure to zonal velocity at the equator is (Moore and Philander 1977)

$$\frac{p_{-1n}(0)}{u_{-1n}(0)} = c_n.$$

But for a Rossby wave, the ratio is

$$\frac{p_{1n}(0)}{u_{1n}(0)} = \frac{c_n}{3}.$$

So we have

$$\frac{u_{1n}(0)}{u_{-1n}(0)} = 3\frac{p_{1n}(0)}{p_{-1n}(0)}.$$

Therefore, for a situation where Rossby and Kelvin wave pressures may be comparable, Rossby waves will explain much more variance in zonal currents along the equator than Kelvin waves.

c. Boundary reflections

In the preceding section, we made the assumption that the reflection at the eastern and western boundaries was not significant. We now examine this assumption more closely to further support our conclusion that the seasonal variability consists predominantly of wind-forced equatorial waves.

1) WESTERN BOUNDARY

At the western boundary, the amplitudes of reflected Kelvin waves can be estimated from the amplitude of incoming Rossby waves based on equatorial wave theory. As suggested by Cane and Sarachik (1981), the western boundary condition in the long-wave limit can be approximated as

$$\int_{-\infty}^{+\infty} (u_i + u_{-1n})|_{x=X_W}\, dy = 0, \qquad (9)$$

where u_i are incident Rossby waves and u_{-1n} are the reflected Kelvin waves. If the incident variability is dominated by the first baroclinic mode, first meridional mode long Rossby waves, which is the case for the seasonal cycle, then (9) becomes

$$\int_{-\infty}^{+\infty} (u_{11} + u_{-11})|_{x=X_W}\, dy = 0.$$

Based on equatorial wave dynamics (McCreary 1981), we have

$$= (1/2)p_{11}(X_w, y_0, t)\phi_0(y)/[\phi_2(y_0)/2^{1/2} + \phi_0(y_0)],$$

where y_0 is some latitude. For $y_0 = 5°$, we have

$$p_{-11}(X_w, y, t) \approx 0.76p_{11}(X_w, 5°, t)\Phi_0(y). \quad (10)$$

Figure 14b ◯▬ shows averages of seasonal variations in surface dynamic height at 5°N and 5°S from the Levitus climatology. This analysis extends farther west than the TAO data with adequate records for compiling a reliable mean climatology in the far western Pacific. The averaged seasonal variations at 5°N and 5°S have amplitudes of about 2.5 dyn cm at their westernmost extent (150°E). Assuming that these amplitudes extend all the way to the western boundary, the amplitude of the reflected Kelvin wave would be about 1.3 dyn cm as determined from (10). This estimate is based on the assumption that the boundary is straight. Since the real boundary is much more complex, reflection will be less efficient and the resulting Kelvin waves might be even smaller. In addition, these waves will be damped while propagating to the east. We therefore conclude that reflection at the western boundary is not significant relative to seasonal wind-forced variations in the central and eastern Pacific (Fig. 6 ◯▬).

2) EASTERN BOUNDARY

At the eastern boundary, incoming seasonal variability consists mainly of the first two baroclinic-mode Kelvin waves. In the idealized case of a straight meridional boundary, these waves reflect into an infinite sum of symmetric mode long Rossby waves (Moore 1968). Using the formalism in McCreary (1985), we computed the amplitudes of the first 10 reflected waves for each of the four vertical modes and plotted their sum along the equator. In this sum, the first meridional mode Rossby wave accounts for most of the reflected wave variance near the equator. Most of this variance is confined to east of 120°W (Fig. 15 ◯▬).

Adding reflected waves to the interior forced wave solutions shows that in the longitude range 110°W–165°E, where we have been able to compute mean seasonal cycles from the TAO data, eastern boundary reflections make very little impact on the overall structure of the zonal currents and sea level (Fig. 16 ◯▬). These results are consistent with those of previous authors (e.g., Kessler and McCreary 1993; Minobe and Takeuchi 1995) who found that eastern boundary reflections contribute little to surface layer variability in the interior of the basin.

d. Sensitivity to damping

The details of our long equatorial wave simulation depend to a certain extent on the choice of damping coefficients. In this study we set the coefficients using (7) with a 6-month damping timescale for the first baroclinic mode and a 2.5-month damping timescale for the second baroclinic mode. To test sensitivity of our simulations to different coefficients, we reran the model with $r_n = (c_1/c_n)^2$ (24 months)$^{-1}$ as in Minobe and Takeuchi (1995). The model results are very similar to those with the shorter timescale damping given by (7) except that amplitudes are about 20% larger. We favor the stronger damping because the model results match TAO observations better and because stronger damping is consistent with Picaut et al.'s (1993) recommendation for modeling equatorial long waves.

e. Higher baroclinic modes

In order to address the question of whether the solutions have adequately converged after summation over four baroclinic modes, we reran our model to include baroclinic modes 5–10. These higher modes, with lower c_n in (5), are more frictionally controlled than the low modes (see McCreary 1981). Adding modes 5–10 increases the model surface zonal velocity amplitude by at most 10% and model sea level by at most 5% along the equator, with the largest increases where the zonal winds are strongest (centered around 125°W). There is little change in the phase of the model results though. Also, the additional surface velocity variance contributed by these higher baroclinic modes to the model solutions is just a few percent when averaged across 110°W–165°E. These results reinforce the conclusion that the character of the solutions is determined primarily by the lowest baroclinic modes, and in particular modes one and two.

f. Higher meridional modes

We also ran our four baroclinic-mode model with higher meridional mode Rossby waves to determine their contributions to near equatorial variability. The amplitude of the third meridional mode, which is the second gravest hemispherically symmetric mode in pressure and zonal velocity, is only about 7% of the amplitude of the first meridional mode in zonal velocity on the equator. The second and fourth meridional modes, which are hemispherically antisymmetric in pressure and zonal velocity, do not contribute at all to varibility on the equator. However these modes, forced by seasonal wind stress and

wind stress curl variations that are stronger north of the equator than south (Gent 1985;McPhaden et al. 1988), enhance seasonal variations in thermocline depth and dynamic height at 5°N relative to those at 5°S. The resultant changes in amplitude are less than 10% and too small to simulate the observed hemispheric asymmetries. Nonetheless, addition of the first two even numbered meridional Rossby modes leads to slightly more realistic results at 5°N and 5°S.

5. Discussion and conclusions

Time series over the period of 1988–96 from the TAO array have been used to document well-defined mean climatologies of surface winds, temperatures, and currents in the equatorial Pacific. Through analysis of these climatologies, we identify the following features in the seasonal variability: 1) the normally westward South Equatorial Current reverses direction in late boreal spring and early summer in the eastern Pacific; 2) seasonal variations in both the SEC and Equatorial Undercurrent propagate westward; 3) seasonal variations in the 20°C isotherm depth and dynamic height at 5°N and 5°S also propagate westward; but 4) along the equator, variations in 20°C isotherm depth and dynamic height propagate eastward in the eastern and central Pacific. These results are consistent with those from other analyses based on ship board and drifter data.

Diagnostic calculations suggest that at 5°N and 5°S seasonal variations are dominated by the gravest two baroclinic-mode, first meridional mode wind-forced long Rossby waves. At the equator, in addition to these Rossby waves, variability associated with the first two baroclinic-mode wind-forced Kelvin waves was shown to be important. The sum of the Rossby waves and Kelvin waves results in westward propagation in the zonal currents but eastward propagation in thermocline depth and dynamic height along the equator in the eastern and central Pacific.

Our results can be compared and contrasted to those of previous studies that have considered the dynamics of the mean seasonal cycle near the equator. For example, Minobe and Takeuchi (1995) also found that the first two vertical mode wind-forced Kelvin and Rossby waves dominated mean seasonal variability in the equatorial Pacific, and that eastern and western boundary reflections were relatively unimportant. However, they did not address the different direction of phase propagation along the equator for zonal currents, 20°C isotherm depths, and dynamic height.

Yang et al. (1997) proposed a different hypothesis than ours to explain why the seasonal variation of thermocline depth propagates eastward along the equator. When forced by the 1 and 2 cpy harmonics of surface winds, their linear model did not produce the right sense of eastward propagation in upper-layer thickness. So between 150°E and 120°W they added an extra abruptly changing zonal wind patch, which excited an eastward propagating Kelvin wave. However, our results indicate that this extra ad hoc forcing is not necessary to generate eastward propagation in upper-layer thickness (or thermocline depth in our case). An essential difference between our study and theirs is how the winds are projected onto the ocean. In Yang et al., a Gaussian meridional structure was assumed for zonal wind stress, with a 3° radius of deformation. Compared to the actual winds projected onto the Kelvin wave as given by b_{-1n} from (6a), their winds have seasonal variations about 30% too weak on average between 140°E and 160°W and about 10% too strong on average between 160° and 100°W. Both the underestimate in the western Pacific and overestimate in the eastern Pacific would suppress Kelvin wave variability and exaggerate Rossby wave variability. The zonal wind patch they added largely overlapped with the region where their assumed meridional structure for the winds leads to underestimates in annual-period forcing. Our results, in which the actual meridional structures are used for the wind forcing, do not require such adjustments.

As discussed in section 3, the westward SEC reverses its direction in the eastern Pacific in late boreal spring and early summer although surface winds are always easterly. This phenomenon has puzzled scientists for more than a century since Puls (1895) first discovered it. Based on this study and previous studies of the mean circulation in the equatorial Pacific, we suggest that this springtime reversal is the result of a weak westward mean current at the surface, on which seasonal wave variability is superimposed. The weak mean westward surface flow results from upward advection of eastward momentum from the EUC core toward the surface and poleward advection of westward momentum put into the ocean by the mean wind stress (e.g., Philander and Pacanowski 1980; Bryden and Brady 1985; McPhaden and Taft 1988). The nonlinearity that gives rise to this mean circulation pattern is relatively weak, however, and can be thought of qualitatively as a first-order correction to the mean circulation (e.g., McPhaden 1981). Superimposed on this mean circulation are seasonal variations in linear, wind-forced Kelvin waves and Rossby waves. In combination these waves produce a tendency for significant eastward flow in late boreal spring and early summer when the trade winds relax, a tendency that is strong enough to overcome the westward mean flow near the surface. The zonal current reversal propagates westward as a result of the current variations associated with the annual-period Rossby wave. The Rossby wave weakens west of about 160°W as it propagates out of the dominant forcing region (Fig. 5a ⬤) and as it leaks energy into the deep ocean (Lukas and Firing 1985; Kessler and McCreary 1993). Hence, at 170°W where westward mean flow in the SEC is strongest, the springtime reversal is weak or nonexistent. Farther to the west at 165°E where the mean SEC is weak and semiannual variations are pronounced, eastward surface currents are observed to run against the wind in June–August.

Yu et al. (1997) also argued that nonlinearity in the mean circulation and springtime weakening of the southeasterly trades play an important role in the occurrence of springtime reversal in the SEC in the eastern Pacific. However, our interpretation differs in some important respects. Yu et al. concluded that the springtime weakening of the local southeasterly trades in the

eastern Pacific is the primary cause of the reversal, while Kelvin waves excited in the western and central Pacific reduce the strength of the reversal. They did not make a link between the springtime reversal and the annual-period Rossby wave, however, nor did they offer an explanation for the westward propagation of the springtime reversal.

Gu et al. (1997) have recently pointed out that seasonal timescale variations are not stationary in the eastern equatorial Pacific. Using TAO data, they showed that thermocline depth variations at periods near one year were more pronounced in the 1990s than in the 1980s. Our definition of the seasonal cycle, which relies most heavily on data from the 1990s, may therefore contain some biases due to decadal timescale variations like those discussed in Gu et al. These biases, if present, are not a serious concern in general, given the comparability of our seasonal analyses and those based on longer term datasets. However, the implications of this nonstationary for understanding ENSO is a topic worth further consideration. Also, Gu et al. suggested, but did not demonstrate, that changes in seasonal variations between the 1980s and the 1990s were due to changes in wind forcing and equatorial ocean long-wave responses. If our interpretation of the mean seasonal cycle in terms of wind-forced equatorial Kelvin and Rossby waves is correct, the diagnostic framework presented in this paper may provide a means to quantitatively evaluate the role of these processes in modulating of the seasonal cycle in the equatorial Pacific.

In summary, our analysis offers some new insights into seasonal variations in the equatorial Pacific Ocean. The diagnostic model we used is very simple and ignores such processes as wave–mean flow interactions and zonal variations in background state. Also, although we have invoked nonlinearity of the mean state as part of our explanation for the springtime reversal of the SEC, we cannot explicitly compute important nonlinear terms in the zonal momentum balance. Finally, we have concentrated our interpretation primarily on hemispherically symmetric aspects of the seasonal cycle, although there are significant asymmetries, particularly in the eastern Pacific, related to meridional wind stress forcing and hemispheric asymmetries in zonal wind stress and wind stress curl forcing. Thus, there is a need for additional work, particularly with numerical models, to examine in more detail the hypotheses we have proposed in this study.

REFERENCES

Balmaseda, M. A., M. K. Davey, and D. L. T. Anderson, 1995: Decadal and seasonal dependence of ENSO prediction skill. *J. Climate,* **8,** 2705–2715.. Find this article online

Battisti, D. S., and A. C. Hirst, 1989: Interannual variability in the tropical atmosphere–ocean system: Influence of the basic state and ocean geometry. *J. Atmos. Sci.,* **46,** 1687–1711.. Find this article online

Bryden, H. L., and E. C. Brady, 1985: Diagnostic model of the three-dimensional circulation in the upper equatorial Pacific Ocean. *J. Phys. Oceanogr.,* **15,** 1255–1273.. Find this article online

Busalacchi, A. J., and J. J. O'Brien, 1980: The seasonal variability in the tropical Pacific. *J. Phys. Oceanogr.,* **10,** 1929–1952.. Find this article online

—— ,M. J. McPhaden, and J. Picaut, 1994: Variability in equatorial Pacific sea surface topography during the verification phase of the TOPEX/POSEIDON mission. *J. Geophys. Res.,* **99,** 24 725–24 738..

Cane, M. A., and E. S. Sarachik, 1981: The response of a linear baroclinic equatorial ocean to periodic forcing. *J. Mar. Res.,* **39,** 651–693..

Chang, P., 1993: Seasonal cycle of sea surface temperature and mixed layer heat budget in the tropical Pacific Ocean. *Geophys. Res. Lett.,* **20,** 2079–2082..

—— ,1994: A study of the seasonal cycle of sea surface temperature in the tropical Pacific Ocean using reduced gravity models. *J. Geophys. Res.,* **99,** 7725–7741..

Chen, D., L. M. Rothstein, and A. J. Busalacchi, 1994: A hybrid vertical mixing scheme and its application to tropical ocean models. *J. Phys. Oceanogr.,* **24,** 2156–2179.. Find this article online

Davis, R. E., 1976: Predictability of sea surface temperature and sea level pressure anomalies over the North Pacific Ocean. *J. Phys.*

Oceanogr., **6,** 249–266.. Find this article online

Draper, N. R., and H. Smith, 1981: *Applied Regression Analysis.* Wiley, 709 pp..

Gandin, L. S., 1966: *Objective Analysis of Meteorological Fields.* Israel Program for Scientific Translations, 242 pp. First published by Gidrometeorol Izdat, 1963..

Gent, P. R., 1985: The annual cycle in the central equatorial Pacific Ocean. *J. Mar. Res.,* **43,** 743–759..

—— ,K. O'Neill, and M. A. Cane, 1983: A model of the semiannual oscillation in the equatorial Indian Ocean. *J. Phys. Oceanogr.,* **13,** 2148–2160.. Find this article online

Gill, A. E., and A. J. Clarke, 1974: Wind-induced upwelling, coastal currents and sea-level changes. *Deep-Sea Res.,* **21,** 325–345..

Gu, D., S. G. H. Philander, and M. J. McPhaden, 1997: The seasonal cycle and its modulation in the eastern tropical Pacific Ocean. *J. Phys. Oceanogr.,* **27,** 2209–2218.. Find this article online

Halpern, D., 1987: Observations of annual and El Niño thermal and flow variations along the equator at 0° 110°W and 0° 95°W during 1980–1985. *J. Geophys. Res.,* **92,** 8197–8212..

Hayes, S. P., P. Chang, and M. J. McPhaden, 1991: Variability of the sea surface temperature in the eastern equatorial Pacific during 1986–88. *J. Geophys. Res.,* **96,** 10 553–10 566..

Hirst, A. C., 1988: Slow instabilities in tropical ocean basin–global atmosphere models. *J. Atmos. Sci.,* **45,** 830–852.. Find this article online

Horel, J. D., 1982: On the annual cycle in the tropical Pacific atmosphere and ocean. *Mon. Wea. Rev.,* **110,** 1863–1878.. Find this article online

Kessler, W. S., 1990: Observations of long Rossby waves in the northern tropical Pacific. *J. Geophys. Res.,* **95,** 5183–5217..

—— ,and J. P. McCreary, 1993: The annual wind-driven Rossby wave in the subthermocline equatorial Pacific. *J. Phys. Oceanogr.,* **23,** 1192–1207.. Find this article online

—— ,and M. J. McPhaden, 1995: Oceanic equatorial waves and the 1991–93 El Niño. *J. Climate,* **8,** 1758–1774.. Find this article online

—— ,—— ,and K. M. Weickmann, 1995: Forcing of intraseasonal Kelvin waves in the equatorial Pacific. *J. Geophys. Res.,* **100,** 10 613–10 631..

Kindle, J. C., 1979: Equatorial Pacific Ocean variability—Seasonal and El Niño time scales. Ph.D. dissertation, The Florida State University, 104 pp..

Latif, M., and N. E. Graham, 1992: How much predictive skill is contained in the thermal structure of an oceanic GCM? *J. Phys. Oceanogr.,* **22,** 951–962.. Find this article online

—— ,T. P. Barnett, M. A. Cane, M. Fluegel, N. E. Graham, H. von Storch, J.-S. Xu, and S. E. Zebiak, 1994: A review of ENSO prediction studies. *Climate Dyn.,* **9,** 167–179..

Legler, K. M., 1991: Producing surface wind products for oceanographers. *Proc. IGOSS/IOC Ocean Products Workshop,* Tokyo, Japan, Intergovernmental Oceanic Commission, 59–76..

Levitus, S., R. Burgett, and T. P. Boyer, 1994a: *World Ocean Atlas 1994.* Vol. 3, *Salinity,* National Oceanic and Atmospheric Administration, 99 pp..

—— ,T. P. Boyer, and J. Antonov, 1994b: *World Ocean Atlas 1994.* Vol. 4, *Temperature,* National Oceanic and Atmospheric Administration, 129 pp..

Li, T., and S. G. H. Philander, 1996: On the annual cycle of the eastern equatorial Pacific. *J. Climate,* **9,** 2986–2998.. Find this article online

Lukas, R., and E. Firing, 1983: The geostrophic balance of the Pacific Equatorial Undercurrent. *Deep-Sea Res.,* **31,** 61–66..

—— ,and —— ,1985: The annual Rossby wave in the central equatorial Pacific Ocean. *J. Phys. Oceanogr.,* **15,** 55–67.. Find this article online

Mangum, L. J., H. P. Freitag, and M. J. McPhaden, 1994: TOGA-TAO array sampling schemes and sensor evaluations. *Proc. Oceans '94 OSATES,* Vol. II, Brest, France, Marine Technology Society, 402–406..

McCarty, M. E., and M. J. McPhaden, 1993: Mean seasonal cycles and interannual variations at 0°, 165°E during 1986–1992. NOAA Tech. Memo. ERL-PMEL-98, Pacific Marine Enviromental Laboratory, Seattle, WA, 64 pp..

McCreary, J., 1981: A linear stratified ocean model of the equatorial undercurrent. *Philos. Trans. Roy. Soc. London,* **298,** 603–645..

—— , 1984: Equatorial beams. *J. Mar. Res.,* **42,** 395–430..

—— , 1985: Modelling equatorial oceanic circulation. *Annu. Rev. Fluid Mech.,* **17,** 359–409..

—— , and R. Lukas, 1986: The response of the equatorial ocean to a moving wind field. *J. Geophys. Res.,* **91,** 11 691–11 705..

McPhaden, M. J., 1981: Continuously stratified models of the steady state equatorial ocean. *J. Phys. Oceanogr.,* **11,** 337–354.. Find this article online

—— , 1993: TOGA-TAO and the 1991–1993 El Niño–Southern Oscillation event. *Oceanogr.,* **6,** 36–44..

—— , 1995: The Tropical Atmosphere Ocean array is completed. *Bull. Amer. Meteor. Soc.,* **76,** 739–741.. Find this article online

—— , and B. A. Taft, 1988: Dynamics of seasonal and intraseasonal variability in the eastern equatorial Pacific. *J. Phys. Oceanogr.,* **18,** 55–67.. Find this article online

—— , and M. E. McCarty, 1992: Mean seasonal cycles and interannual variations at 0°, 110°W and 0°, 140°W during 1980–1991. NOAA Tech. Memo. ERL-PMEL-95, Pacific Marine Enviromental Laboratory, Seattle, WA, 118 pp..

—— , J. A. Proehl, and L. M. Rothstein, 1987: On the structure of low frequency equatorial waves. *J. Phys. Oceanogr.,* **17,** 1555–1559.. Find this article online

—— , A. J. Busalacchi, and J. Picaut, 1988: Observations and wind forced model simulations of the mean seasonal cycle in tropical Pacific sea surface topography. *J. Geophys. Res.,* **93,** 8131–8146..

Mechoso, C. R., and Coauthors, 1995: The seasonal cycle over the tropical Pacific in coupled ocean–atmosphere general circulation models. *Mon. Wea. Rev.,* **123,** 2825–2838.. Find this article online

Meyers, G., 1979a: Annual variation in the slope of the 14°C isotherm along the equator in the Pacific Ocean. *J. Phys. Oceanogr.,* **9,** 885–891.. Find this article online

—— , 1979b: On the annual Rossby wave in the tropical North Pacific Ocean. *J. Phys. Oceanogr.,* **9,** 663–674.. Find this article online

—— , and J.-R. Donguy, 1980: An XBT network with merchant ships. *Trop. Ocean–Atmos. Newslett.,* **2,** 6–7..

Minobe, S., and K. Takeuchi, 1995: Annual period equatorial waves in the Pacific Ocean. *J. Geophys. Res.,* **100** (C9), 18 379–18 392..

Moore, D. W., 1968: Planetary-gravity waves in an equatorial ocean. Ph.D. thesis, Harvard University..

—— , and S. G. H., Philander, 1977: Modelling of the tropical oceanic circulation. *The Sea,* Vol. 6, E. D. Goldberg, I. N. McCave, J. J. O'Brien, and J. H. Steele, Eds., John Wiley and Sons, 319–361..

Philander, S. G. H. and R. Pacanowski, 1980: The generation of equatorial currents. *J. Geophys. Res.,* **85** (C2), 1123–1136..

—— , and Y. Chao, 1991: On the contrast between the seasonal cycles of the equatorial Atlantic and Pacific Oceans. *J. Phys. Oceanogr.,* **21,** 926–931.. Find this article online

—— , W. J. Hurlin, and A. D. Seigel, 1987: Simulation of the seasonal cycle of the tropical Pacific Ocean. *J. Phys. Oceanogr.,* **17,** 1986–2002.. Find this article online

Picaut, J., C. Menkes, J. P. Boulanger, and Y. Penhoat, 1993: Dissipation in a Pacific equtorial long wave model. TOGA Notes, Nova University, Dania, FL, 11–15..

Plimpton, P. E., H. P. Freitag, and M. J. McPhaden, 1997a: ADCP velocity errors from pelagic fish schooling around equatorial moorings. *J. Atmos. Oceanic Technol.,* **14,** 1212–1223..

—— , —— , —— , and R. H. Weisberg, 1997b: Using echo intensity to correct moored ADCP data for fish-bias errors at 0°, 170°W. NOAA Tech. Memo. ERl-PMEL-111, Pacific Marine Enviromental Laboratory, Seattle, WA, 163 pp..

Puls, C., 1895: Oberflachentemperaturen und Stromungsverhaltmisse des Aquatorialgurtels des Stillen Ozeans. *Dtsch. Arch. Seewarte,* **18,** 1–38..

Rasmusson, E. M., and T. Carpenter, 1982: Variations in tropical sea surface temperature and surface wind fields associated with the Southern Oscillation/El Niño. *Mon. Wea. Rev.,* **110,** 354–384.. Find this article online

Reverdin, G., C. Frankignoul, E. Kestenare, and M. J. McPhaden, 1994: Seasonal variability in the surface currents of the equatorial Pacific. *J. Geophys. Res.,* **99,** 20 323–20 343..

Reynolds, R. W., and T. M. Smith, 1995: A high resolution global sea surface temperature climatology. *J. Climate,* **8,** 1571–1583.. Find this article online

Seager, R., S. E. Zebiak, and M. A. Cane, 1988: A model of the tropical sea surface temperature climatology. *J. Geophys. Res.,* **93,** 1265–1280..

Webster, P. J., and S. Yang, 1992: Monsoon and ENSO: Selectively interactive systems. *Quart. J. Roy. Meteor. Soc.,* **118,** 877–926..

Weisberg, R. H., and S. P. Hayes, 1995: Upper ocean variability on the equator in the west-central Pacific at 170°W. *J. Geophys. Res.,* **100,** 20 485–20 498..

Xie, S.-P., 1995: Interaction between the annual and interannual variations in the equatorial Pacific. *J. Phys. Oceanogr.,* **25,** 1930–1941.. Find this article online

Yang, Y. J., T. Y. Tang, and R. H. Weisberg, 1997: Basin-wide zonal wind stress and ocean thermal variations in the equatorial Pacific Ocean. *J. Geophys. Res.,* **102,** 911–927..

Yu, Z., P. S. Schopf, and J. P. McCreary, 1997: On the annual cycle of upper ocean circulation in the eastern equatorial Pacific. *J. Phys. Oceanogr.,* **27,** 309–324.. Find this article online

Tables

Table 1. Estimated zonal phase speeds (m s^{-1}) of the annual harmonics for mean climatologies. The speeds are derived from an amplitude weighted mean least squares regression of phases along the equator. One standard error is indicated for each estimate.

TAO climatologies		
τ^x		-0.43 ± 0.13
$u_{10\,m}$		-0.73 ± 0.27
$u_{80\,m}$		-1.13 ± 0.45
SST		-0.87 ± 0.23
20°C depth	$y = 0°$	$0.65 \pm 0.21*$
	$y = 5°N$	-1.11 ± 0.37
	$y = 5°S$	-0.90 ± 0.55
Surface dynamic height	$y = 0°$	$0.49 \pm 0.18*$
	$y = 5°N$	-0.92 ± 0.29
	$y = 5°S$	-0.85 ± 0.67
Other climatologies		
FSU τ^x		-0.38 ± 0.06
Reverdin u		-0.59 ± 0.08
Reynolds SST		-0.68 ± 0.09
Levitus 20°C depth	$y = 0°$	$0.67 \pm 0.21*$
	$y = 5°N$	-0.97 ± 0.17
	$y = 5°S$	-0.83 ± 0.16
Levitus surface dynamic height	$y = 0°$	$0.47 \pm 0.15*$
	$y = 5°N$	-1.00 ± 0.20
	$y = 5°S$	-0.76 ± 0.38

* Fit only to longitudes 155°W–110°W.

Click on thumbnail for full-sized image.

Table 2. The values of baroclinic mode parameters for the first four modes based on data from Hawaii–Tahiti Shuttle experiment 150°–158°W.

	Mode 1	Mode 2	Mode 3	Mode 4
Equivalent depth H_n (cm)	76.0	30.9	11.5	5.9
Wave speed $c_n = (gH_n)^{1/2}$ (m s^{-1})	2.73	1.74	1.06	0.76
Rossby radius $R = (c_n/\beta)^{1/2}$ (km)	346	276	216	183

Click on thumbnail for full-sized image.

## Figures
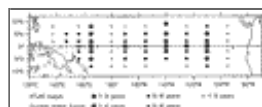
Click on thumbnail for full-sized image.

Fig. 1. The TAO array as of December 1996. Circles are ATLAS thermistor chain buoys, while squares indicate current meter

moorings. The size of the symbols indicates length of time a buoy has been in the water at each location.
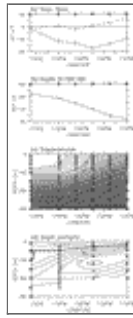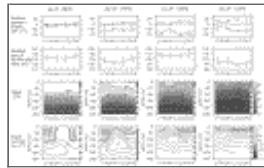

Click on thumbnail for full-sized image.

Fig. 2. Longitudinal structure of mean fields at the equator from TAO observations. (a) Surface zonal (solid) and meridional (dashed) pseudostress τ^x, τ^y (m^2 s^{-2}). Vertical bars are 90% confidence intervals. (b) Surface dynamic height relative to 500 db (dyn. cm). (c) Temperature (°C); 90% confidence limits are ±0.3, ±0.7, and ±0.2°C above, at, and below the thermocline, respectively. (d) Zonal currents (cm s^{-1}); 90% confidence limits are ±7, ±9, and ±4 cm s^{-1} above, at, and below the EUC core, respectively. Small squares indicate locations of measurements. ADCP resolution at 0°, 170°W is 10 m; only every other 10-m measurement depth is shown. Westward flow is shaded.
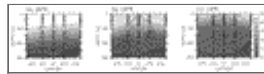
Click on thumbnail for full-sized image.

Fig. 3. Latitudinal structure of mean temperature field from TAO observations along 110°W, 140°W, and 165°E; 90% confidence limits are the same as in Fig. 2 ⊙. Small squares indicate locations of measurements.

Click on thumbnail for full-sized image.

Fig. 4. Monthly mean climatologies of surface pseudostress (m^2 s^{-2}), surface dynamic height relative to 500 db (dyn cm), temperature (°C), and zonal currents (cm s^{-1}) at (a) 0°, 165°E, (b) 0°, 170°W, (c) 0°, 140°W, and (d) 0°, 110°W. Ninety percent confidence intervals are indicated every third month for winds and dynamic heights. Shading indicates westward flow. Small squares indicate locations of measurements.
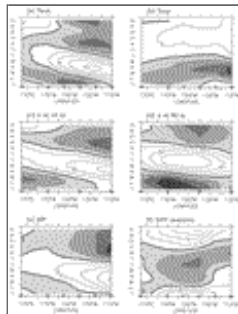
Click on thumbnail for full-sized image.

Fig. 5. De-meaned seasonal variations along the equator from TAO array observations. (a) Zonal pseudostress (m^2 s^{-2}); (b) meridional pseudostress (m^2 s^{-2}); (c) zonal current at 10 m (cm s^{-1}); (d) zonal current at 80 m (cm s^{-1}); (e) SST (°C); and (f) depth of 20°C isotherm (m). The squares on the lower axis are measurement longitudes. Negative anomalies are shaded.
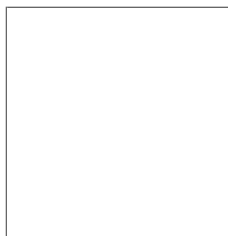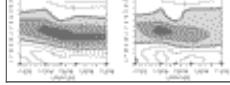
Fig. 6. De-meaned seasonal variations along the equator from TAO observations. Left panels: depth of 20°C isotherm (m); and right panels: surface dynamic height relative to 500 db (dyn cm). The squares on the lower axis are measurement longitudes. Negative anomalies are shaded.
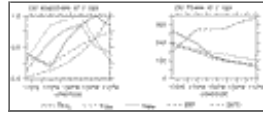
Fig. 7. Amplitudes and phases of 1 cpy harmonic based on least squares regression analysis of TAO data. Solid line: pseudostress τ^x; short dashed line: u_{10m}; dotted line: u_{80m}; dotted–dashed line: SST; long dashed line: 20°C isotherm. Amplitudes are each normalized by their maximum. $\tau^x_{max} = 9.6$ m^2 s^{-2}; $u_{max} = 0.37$ m s^{-1}; SST$_{max} = 2.0$°C; and D$^{20°C}_{max} = 19.4$ m. Dynamic height (not shown) has a structure very similar to that of 20°C.
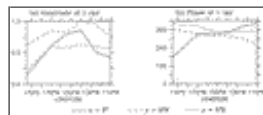
Fig. 8. Amplitudes and phases of 1 cpy harmonic based on least squares regression analysis of 20°C isotherm depth from TAO data. Solid line: $y = 0$°; dashed line: $y = 5$°N; and dotted line: $y = 5$°S. Amplitudes are normalized $D^{20°C}_{max} = 19.4$ m. Dynamic height (not shown) has a structure very similar to that of 20°C.
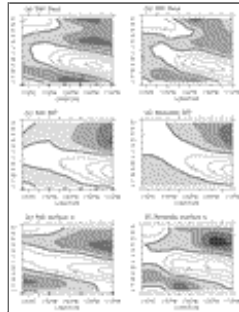
Fig. 9. Comparison of de-meaned seasonal variability between TAO and other datasets along the equator. Squares on the lower axis are measurement longitudes for TAO. The negative is shaded. (a), (b): zonal pseudostress τ^x from TAO and FSU (m^2 s^{-2}); (c), (d): SST from TAO and Reynolds and Smith (1995). (°C); and (e), (f): surface zonal current from TAO and Reverdin et al. (1994) (cm s^{-1}).
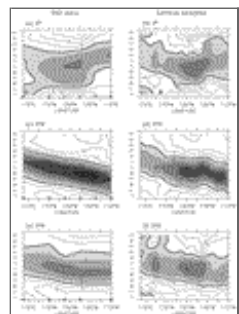
Fig. 10. Comparison of de-meaned seasonal variability in 20°C isotherm depth between TAO and Levitus datasets. Squares on the lower axis are measurement for TAO. Contour intervals are 5 m. Negative anomalies (shading) means shoaling. Left panels: TAO data, and right panels: Levitus data.
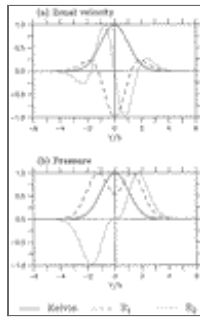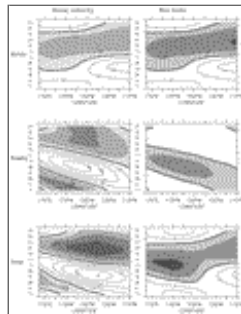
Click on thumbnail for full-sized image.

Fig. 11. Meridional structures of equatorial waves. Amplitudes are normalized and y axis is nondimensionalized by the Rossby radius of deformation given by Eq. (4). (a) Zonal velocity; (b) pressure. Solid: Kelvin wave; dashed: first meridional mode Rossby wave; dotted: second meridional mode Rossby wave. See Table 2 ⬤▬ for dimensional values of the Rossby radii.
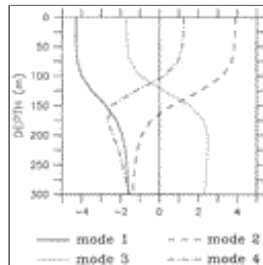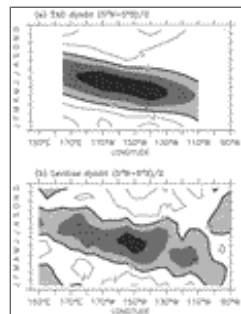

Click on thumbnail for full-sized image.

Fig. 12. Vertical profiles of the first four baroclinic modes for horizontal velocity components and pressure based on data from the Hawaii–Tahiti Shuttle experiment 150°–158°W. Solid: first mode; dashed: second mode; dotted: third mode; dashed–dotted: fourth mode.

Click on thumbnail for full-sized image.

Fig. 13. Kelvin and Rossby waves in zonal surface current and sea level and their combination at seasonal cycle from the model. Upper panels: sum of the four gravest baroclinic mode Kelvin waves; middle panels: sum of the four gravest baroclinic mode, first meridional mode Rossby waves; lower panels: combination of Kelvin and Rossby waves. Contour intervals for zonal current and sea level are 10 cm s^{-1} and 2 cm.

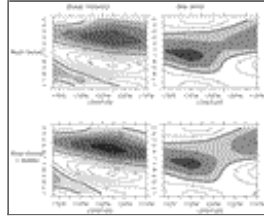Click on thumbnail for full-sized image.

Fig. 14. Mean seasonal cycle of dynamic height average for 5°N and 5°S. (a) TAO observations; (b) Levitus analysis. Negative anomalies are shaded. Contour interval is 2 dyn cm.
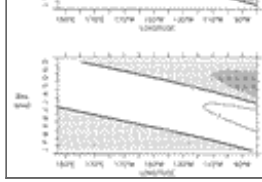
Fig. 15. Reflected Rossby waves from the eastern boundary. Upper panel: zonal surface velocity; lower panel: sea level. Contour intervals for zonal velocity and sea level are 10 cm s^{-1} and 1 cm.

Fig. 16. Comparison of simulated seasonal variability in zonal surface current and sea level with and without eastern boundary reflection. Upper panels: sum of seasonal Kelvin and Rossby waves directly forced by surface wind stress; lower panels: the combination of variability in the upper panels and reflected Rossby waves in Fig. 15 ⊙. Contour intervals for zonal current and sea level are 10 cm s^{-1} and 2 cm.